CONDENSED MATTER PHYSICS

2016 © The Authors, some rights reserved; exclusive licensee American Association for the Advancement of Science. Distributed under a Creative Commons Attribution NonCommercial License 4.0 (CC BY-NC).
10.1126/sciadv.1600295

A strongly robust type II Weyl fermion semimetal state in Ta_3S_2

Guoqing Chang,[1,2]* Su-Yang Xu,[3]*† Daniel S. Sanchez,[3] Shin-Ming Huang,[1,2] Chi-Cheng Lee,[1,2] Tay-Rong Chang,[3,4] Guang Bian,[3] Hao Zheng,[3] Ilya Belopolski,[3] Nasser Alidoust,[3] Horng-Tay Jeng,[4,5] Arun Bansil,[6] Hsin Lin,[1,2]† M. Zahid Hasan[3]†

Weyl semimetals are of great interest because they provide the first realization of the Weyl fermion, exhibit exotic quantum anomalies, and host Fermi arc surface states. The separation between Weyl nodes of opposite chirality gives a measure of the robustness of the Weyl semimetal state. To exploit the novel phenomena that arise from Weyl fermions in applications, it is crucially important to find robust separated Weyl nodes. We propose a methodology to design robust Weyl semimetals with well-separated Weyl nodes. Using this methodology as a guideline, we search among the material parameter space and identify by far the most robust and ideal Weyl semimetal candidate in the single-crystalline compound tantalum sulfide (Ta_3S_2) with new and novel properties beyond TaAs. Crucially, our results show that Ta_3S_2 has the largest *k*-space separation between Weyl nodes among known Weyl semimetal candidates, which is about twice larger than the measured value in TaAs and 20 times larger than the predicted value in WTe_2. Moreover, all Weyl nodes in Ta_3S_2 are of type II. Therefore, Ta_3S_2 is a type II Weyl semimetal. Furthermore, we predict that increasing the lattice by <4% can annihilate all Weyl nodes, driving a novel topological metal-to-insulator transition from a Weyl semimetal state to a topological insulator state. The robust type II Weyl semimetal state and the topological metal-to-insulator transition in Ta_3S_2 are potentially useful in device applications. Our methodology can be generally applied to search for new Weyl semimetals.

INTRODUCTION

The rich correspondence between high-energy particle physics and low-energy condensed matter physics has been a constant source of inspiration throughout the history of modern physics (*1*). This has led to important breakthroughs in many aspects of fundamental physics, such as the Planck constant and blackbody radiation, the Pauli exclusion principle and magnetism, and the Anderson-Higgs mechanism and superconductivity, which, in turn, helped us understand materials that can lead to important practical applications. Recently, there has been significant interest in realizing high-energy particles in solid-state crystals. The discovery of massless Dirac fermions in graphene and on the surface of topological insulators has taken the center stage of research in condensed matter and materials science for the past decade (*2*–*5*). Weyl semimetals (*6*–*21*) are crystals whose quasi-particle excitation is the Weyl fermion (*6*), a particle that played a crucial role in the development of quantum field theory and the Standard Model but has not yet been observed as a fundamental particle in nature. Weyl fermions have a definite left- or right-handed chirality and can be combined in pairs of opposite chirality to generate a massless Dirac fermion. In a Weyl semimetal, the chirality associated with each Weyl node can be understood as a topologically protected charge, thus broadening the classification of topological phases of matter beyond insulators. The presence of parallel electric and magnetic fields can break the apparent conservation of the chiral charge, which results in the condensed matter version of the chiral anomaly, making a Weyl semimetal, unlike ordinary nonmagnetic metals, more conductive with an increasing magnetic field (*22*, *23*). Weyl nodes are extremely robust against imperfections in the host crystal and are protected by the crystals' inherent translational invariance (*12*). This gives rise to an exceptionally high electron mobility, suggesting that Weyl semimetals may be used to improve electronics by more efficiently carrying electric currents (*24*). Because Weyl fermion quasi-particles are naturally spin-momentum locked (*12*, *14*, *15*) and superconductivity in these materials may exhibit non-Abelian statistics (*25*–*27*), they may also be exploited to realizing new applications, such as in spintronics and quantum computers. Furthermore, a monolayer [the two-dimensional (2D) limit] of time-reversal breaking Weyl semimetals can host quantized anomalous Hall (or spin Hall) current without an external magnetic field. To make these novel phenomena experimentally accessible, especially under ambient conditions so that they can be used in device applications, a robust Weyl semimetal with well-seperated Weyl nodes is critically needed.

Recently, the first Weyl semimetal was discovered in the TaAs (tantalum arsenide) family (*17*–*19*, *21*, *28*–*37*). However, research progress is still significantly held back because of the lack of robust and ideal material candidates. In a Weyl semimetal, Weyl nodes of opposite chirality are separated in momentum space. The degree of separation between Weyl nodes provides a measure of the "topological strength" of the Weyl phase (*38*) that one has to overcome to annihilate the Weyl fermions in pairs. A large *k*-space separation of the Weyl nodes gurantees a robust and stable Weyl semimetal state, which is a prerequisite for observing the many exotic phenomena predicted to be detectable in spectroscopic and transport experiments. Therefore, it is of critical importance to find robust and ideal Weyl semimetals, which have fewer

[1]Centre for Advanced 2D Materials and Graphene Research Centre, National University of Singapore, 6 Science Drive 2, Singapore 117546, Singapore. [2]Department of Physics, National University of Singapore, 2 Science Drive 3, Singapore 117542, Singapore. [3]Laboratory for Topological Quantum Matter and Spectroscopy (B7), Department of Physics, Princeton University, Princeton, NJ 08544, USA. [4]Department of Physics, National Tsing Hua University, Hsinchu 30013, Taiwan. [5]Institute of Physics, Academia Sinica, Nankang, Taipei 11529, Taiwan. [6]Department of Physics, Northeastern University, Boston, MA 02115, USA.
*These authors contributed equally to this work.
†Corresponding author. Email: suyangxu@princeton.edu (S.-Y.X.); nilnish@gmail.com (H.L.); mzhasan@princeton.edu (M.Z.H.)

Downloaded from http://advances.sciencemag.org/ on September 26, 2017

Weyl nodes and more importantly whose Weyl nodes are well separated in momentum space and are located near the chemical potential in energy.

Moreover, in contrast to the Weyl fermions in high-energy physics, which travel exactly at the speed of light and strictly obey Lorentz invariance, the emergent Weyl fermions in a Weyl semimetal are not subject to these restrictions. It has been recently proposed that the emergent Weyl fermions in a Weyl semimetal can be classified into two types (*39*). The type I Weyl fermions, which have been realized in TaAs (*17*–*19*, *21*, *28*–*37*), respect Lorentz symmetry and have a typical conical dispersion. On the other hand, the type II Weyl fermions strongly violate Lorentz symmetry and manifest in a tilted-over cone in energy-momentum space. Such a type II Weyl semimetal state not only provides a material platform for testing exotic Lorentz-violating theories beyond the Standard Model in tabletop experiments but also paves the way for studying novel spectroscopic and transport phenomena specific to type II Weyl fermions, including the chiral anomaly (whose transport response strongly depends on the direction of the electric current), an antichiral effect of the chiral Landau level, a modified anomalous Hall effect, and emergent Lorentz invariant properties due to electron-electron interaction (*38*–*41*). To date, the type II Weyl semimetal state has only been suggested in $W_{1-x}Mo_xTe_2$ (*38*, *39*) and observed in LaAlGe (*41*). Therefore, it is of importance to search for new type II Weyl semimetals.

Here, we propose a methodology to design and search for robust Weyl semimetals with well-separated Weyl nodes. Using this methodology as a guideline, we identify by far the most robust and ideal Weyl semimetal candidate in the single-crystalline compound tantalum sulfide (Ta_3S_2) with new and novel properties beyond TaAs. Crucially, our results show that Ta_3S_2 has the largest *k*-space separation between Weyl nodes among known Weyl semimetal candidates, which is about twice larger than the measured value in TaAs and 20 times larger than the predicted value in WTe_2. Moreover, all Weyl nodes in Ta_3S_2 are of type II. Therefore, Ta_3S_2 is a type II Weyl semimetal. We further predict a novel topological metal-to-insulator transition from a Weyl semimetal state to a topological insulator state in Ta_3S_2. The robust type II Weyl semimetal state and the topological metal-to-insulator transition in Ta_3S_2 are potentially useful in device applications. Our methodology can be generally applied to search for new Weyl semimetals.

RESULTS

We start by describing our methodology to design robust Weyl semimetals using well-separated Weyl nodes. It has been widely accepted that strong spin-orbit coupling (SOC) is a key ingredient to realizing topological states. Our methodology evades this commonly accepted point of view. We show that, to design robust Weyl semimetals with well-separated Weyl nodes, one needs to look for materials (i) that break space-inversion symmetry, (ii) that have small density of states (DOS) at the chemical potential, and (iii) that are already a Weyl semimetal in the absence of SOC. SOC, on the other hand, does not play a significant role in the whole consideration. We elaborate on our methodology in Fig. 1. Figure 1 (A and B) shows the previous way of looking for Weyl semimetals. Specifically, without SOC, the conduction and valence bands show some nodal crossings (which are not Weyl nodes). The inclusion of SOC splits each nodal point into a pair of Weyl nodes of opposite chiralities. In this way, the separation between the Weyl nodes is entirely determined by the SOC strength of the compound. For example, the first and the only Weyl semimetal in experiments, TaAs, belongs to this type (*17*, *19*). TaAs has almost the strongest SOC that one could achieve in real materials. Even then, the separation was only barely resolved in experiments (*19*). Finding Weyl semimetals with larger separation than TaAs using the previous method is not possible. By contrast, in Fig. 1 (C and D), we present a new methodology. We propose to look for compounds that are already a Weyl semimetal without SOC (Fig. 1C). The inclusion of SOC will split each Weyl node into two nodes of the same chirality. In this way, SOC becomes irrelevant. The separation between the Weyl nodes of opposite chiralities is determined by the magnitude of the band inversion, which is not limited by the SOC strength and can be very large. Therefore, our new methodology can give rise to robust Weyl semimetals with well-separated Weyl nodes.

Using this methodology as a guideline, we have searched among the material parameter space and identified by far the most robust and ideal

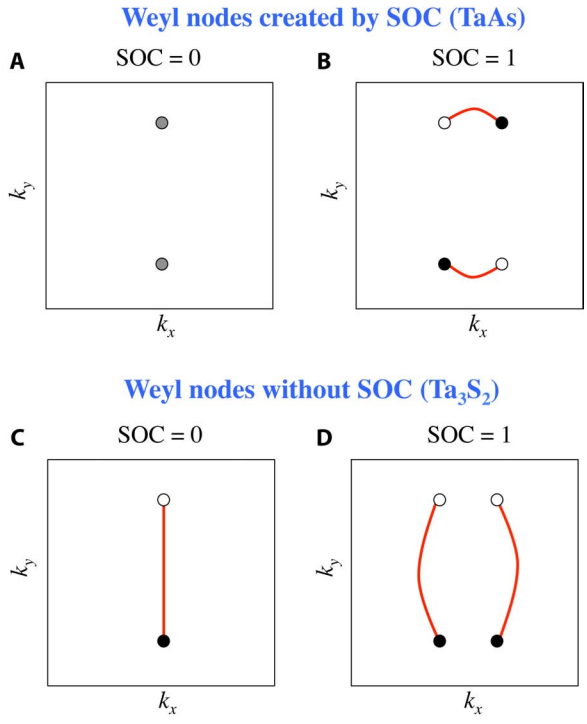

Fig. 1. Methodology to design robust Weyl semimetals with well-separated Weyl nodes. (**A** and **B**) The previous way of looking for Weyl semimetal states. Without SOC, the conduction and valence bands show some nodal crossings (which are not Weyl nodes). The inclusion of SOC splits each nodal point into a pair of Weyl nodes of opposite chiralities. In this way, the separation between the Weyl nodes is entirely determined by the SOC strength of the compound. For example, the first and the only Weyl semimetal in experiments, TaAs, belongs to this type (*17*, *19*). In the absence of SOC, the conduction and valence bands cross each other to form nodal lines. The inclusion of SOC gaps out the nodal lines and gives rise to 12 pairs of Weyl nodes (*19*). (**C** and **D**) Our new methodology to design robust Weyl semimetals with well-separated Weyl nodes. We propose to look for compounds that are already Weyl semimetals without SOC. The inclusion of SOC will split each Weyl node into two nodes of the same chirality. In this way, SOC becomes irrelevant. The separation between the Weyl nodes of opposite chiralities is determined by the magnitude of the band inversion, which is not limited by the SOC strength and can be very large.

Downloaded from http://advances.sciencemag.org/ on September 26, 2017

Weyl semimetal candidate in the inversion-breaking, single-crystalline compound Ta_3S_2 with new and novel properties beyond TaAs. Ta_3S_2 crystallizes in a base-centered orthorhombic structure (*42*, *43*). Single crystals of this compound have been grown (*42*, *43*), and transport experiments have indeed reported a semimetallic behavior (*42*). The lattice constants are a = 5.6051 Å, b = 7.4783 Å, and c = 17.222 Å, and the space group is *Abm*2 (# 39). There are 24 Ta atoms and 16 S atoms in a conventional unit cell (Fig. 2, A and B). It can be seen that the lattice lacks space-inversion symmetry, which is key to realizing the Weyl semimetal state in this time-reversal invariant system. Moreover, the system has two glide mirror symmetries associated with the y and z directions, that is, $\mathcal{G}_y$: $(x, y, z) \Rightarrow (x, -y, z + 0.5)$ and $\mathcal{G}_z$: $(x, y, z) \Rightarrow (x, y, -z + 0.5)$, but it does not have any mirror symmetry along the x direction. The symmetry condition determines the number, energy, and momentum space configuration of the Weyl nodes in Ta_3S_2, which will be discussed below.

Figure 2 (D and F) shows the first-principles calculated band structure in the absence of SOC, from which it can be seen that the conduction and valence bands dip into each other, suggesting a semimetallic ground state. Particularly, we find that the conduction and valence bands cross each other without opening up a gap along the X-Γ-Z-X_1 direction. Upon the inclusion of SOC (Fig. 2, E and G),

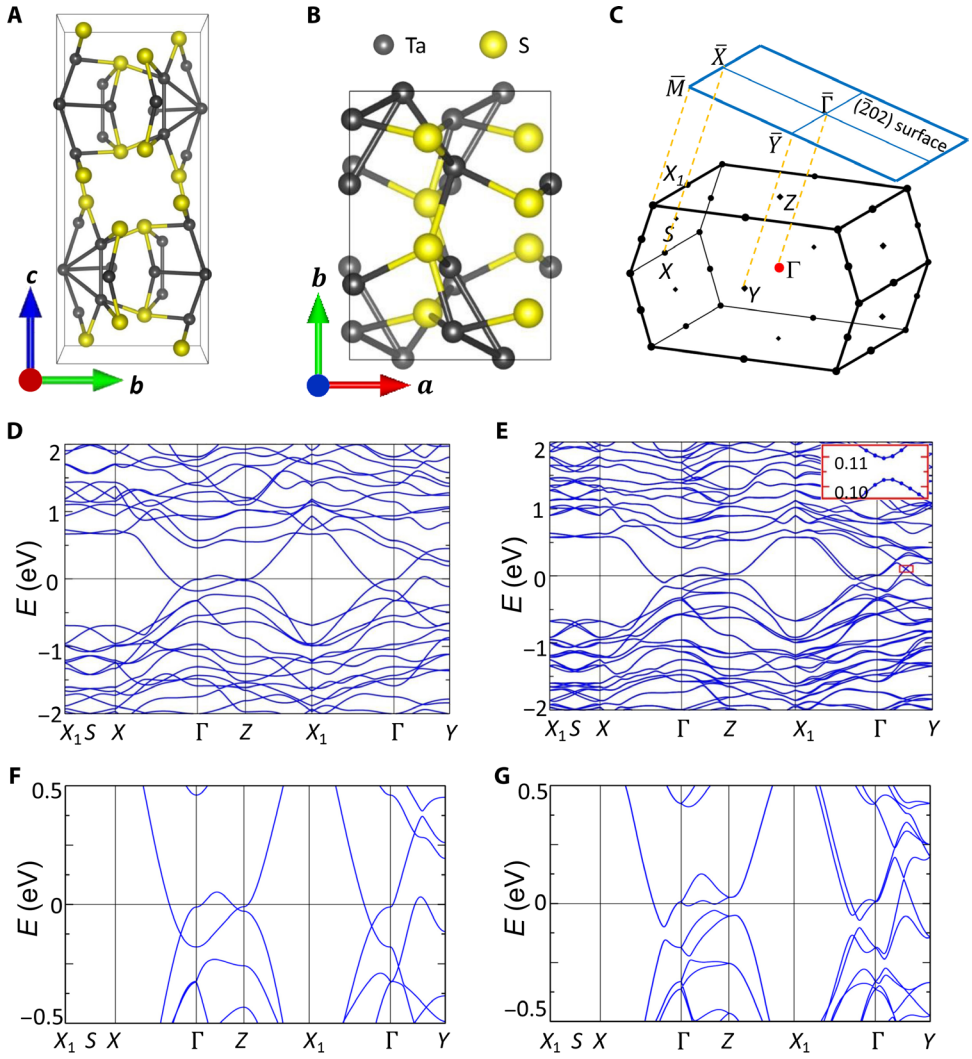

Fig. 2. Crystal and band structure of Ta_3S_2. (**A**) Side view of the crystal structure for one unit cell of Ta_3S_2. The dark gray and yellow balls represent the Ta and S atoms, respectively. (**B**) Same as (A) but for the top view. Ta_3S_2 crystallizes in a base-centered orthorhombic structure with space group *Abm*2 (# 39) with lattice constants a = 5.6051 Å, b = 7.4783 Å, and c = 17.222 Å. As can be seen from the crystal lattice structure, Ta_3S_2 lacks inversion symmetry. (**C**) The primitive first BZ of Ta_3S_2 showing a base-centered orthorhombic structure and the location of relevant high-symmetry points. Representing the $(\bar{2}02)$ surface is a blue rectangular plane. The yellow dashed lines represent the projection of high-symmetry points on the $(\bar{2}02)$ surface. (**D**) First-principles electronic band structure calculation for Ta_3S_2 in the absence of SOC. Bulk band crossings observed along the Γ-X-Z-X_1 direction line near the Fermi level are a part of a line node on the k_y = 0 plane. (**E**) Same as (D) but with the addition of SOC. After the incorporation of SOC, the band structure is fully gapped along all high-symmetry directions. Zooming into the red box along the Γ-Y direction shows a minimum gap size between the conduction band minimum and the valence band maximum of ≈ 7 meV, which is 96.5% smaller than the 200-meV gap observed along the same direction in (D). (**F** and **G**) Zooming in near the Fermi level for (D) and (E), respectively. Upon the inclusion of SOC, we clearly observe that the band structure becomes fully gapped along all high-symmetry directions.

Downloaded from http://advances.sciencemag.org/ on September 26, 2017

the band structure is found to be fully gapped along all high-symmetry directions.

To search for the Weyl nodes in Ta_3S_2, we calculated the band structure throughout its Brillouin zone (BZ). In the absence of SOC (Fig. 3A), we found a line node on the $k_y = 0$ plane, which is the band crossings along the Γ-X-Z-X_1 direction, as shown in Fig. 2D. This line node is on the $k_y = 0$ plane and is, therefore, protected by the mirror symmetry $\mathcal{G}_y$. In addition, we also found two pairs of Weyl nodes located on the $k_x = 0$ plane (Fig. 3A). We determine the chirality of the Weyl node by computing the Berry curvature through a closed 2D manifold enclosing the node. Considering the available symmetries as discussed above, Ta_3S_2 has only one irreducible pair of Weyl nodes. The second pair is obtained by applying the mirror operation $\mathcal{G}_z$. In general, a mirror symmetry operation reflects a Weyl node on one side of the mirror plane to the mirror-reflected location on the other side while also flipping the sign of the chiral charge. Hence, it can be seen that the two pairs of Weyl nodes without SOC are directly related by the mirror operation $\mathcal{G}_z$. Upon the inclusion of SOC, each Weyl node without SOC splits into two spinful Weyl nodes of the same chirality. This is quite intuitive because each state without SOC should be considered as two states of opposite spins. For this reason, there are four pairs of Weyl nodes in the presence of SOC. Again, there is only one irreducible pair and the others are related by the mirror operations $\mathcal{G}_y$ and $\mathcal{G}_z$. Also, because of the mirror symmetries, all the Weyl nodes have the same energy in Ta_3S_2. We show the dispersion away from a Weyl node along all three momentum space directions in Fig. 3 (C and D). It can be seen that the Weyl nodes in Ta_3S_2 are of type II (*39*), because the two bands that cross to form the Weyl nodes have the same sign of velocity along one momentum direction (in this case, k_y). In the presence of SOC (Fig. 3D), the Weyl nodes are approximately 10 meV below the Fermi level, which is in contrast to the case in $Mo_xW_{1-x}Te_2$ systems (*38*, *39*). This makes Ta_3S_2 more hopeful than $Mo_xW_{1-x}Te_2$ (*38*, *39*) for observing the type II Weyl nodes by photoemission experiments. The k separation of the Weyl nodes (Fig. 3D) in Ta_3S_2 is as large as ~ 0.15 $Å^{-1}$. This is by far the largest among known Weyl semimetal candidates and, in fact, twice larger than the measured value in TaAs (about 0.07 to 0.08 $Å^{-1}$) (*19*) and 20 times larger than the predicted value in WTe_2 (~ 0.007 $Å^{-1}$) (*39*). The fact that the Weyl nodes are well separated in momentum space and the fact that they are located near the chemical potential make Ta_3S_2 by far the most robust and ideal Weyl semimetal candidate for observing and realizing the novel Weyl physics in both spectroscopic and transport experiments.

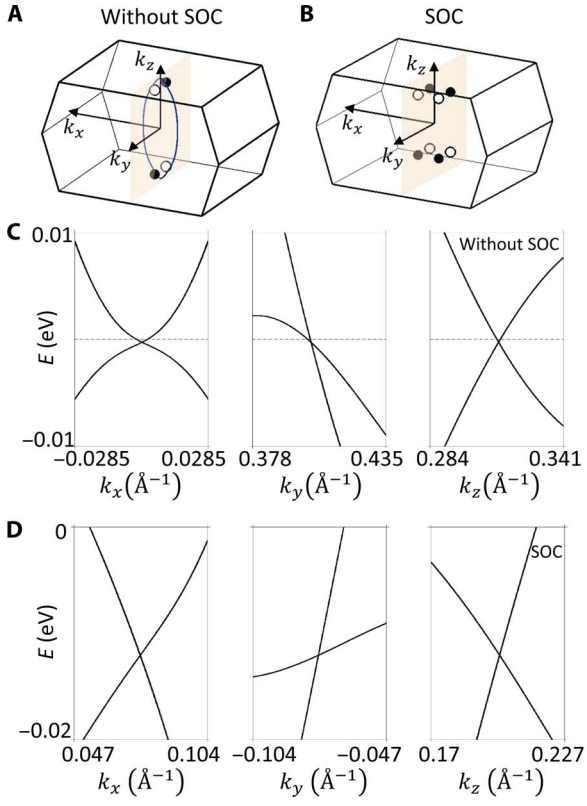

Fig. 3. Weyl nodes in Ta_3S_2. (**A**) The primitive first BZ of Ta_3S_2 showing the k-space location of the Weyl points in the absence of SOC. The black and white circles represent Weyl points with opposite chirality. On the $k_x = 0$ plane, represented in tan, we observe two pairs of Weyl nodes with chiral charge ± 1. Only one pair of Weyl nodes is an irreducible representation. The line node on the $k_y = 0$ plane that corresponds to the crossing along the Γ-X-Z-X_1 direction is shown in blue. (**B**) Same as (A) but after the incorporation of SOC. Each Weyl node splits into two spinful Weyl nodes of the same chirality and moves into the bulk. Therefore, we observe eight Weyl nodes in a single BZ. (**C**) The energy dispersion along the three momentum space directions of the Weyl node in the absence of SOC. (**D**) Same as (C) but with the addition of SOC. From this series of energy dispersion cuts along the three momentum space directions around the Weyl point, its type II character is revealed (that is, observe along k_y that both crossing bands have the same sign of velocity along one momentum direction). Furthermore, observe that the Weyl nodes also move deeper in binding energy, ≈ −10 meV.

Another signature of the Weyl semimetal state is the Fermi arc electron states on the surface of the crystal. Figure 4 shows the calculated surface state electronic structure on the $(\bar{2}02)$ surface of Ta_3S_2. The calculated surface state Fermi surface (Fig. 4, A and D) shows a rich structure, including both topological Fermi arcs and topologically trivial surface states. There are finite projected bulk Fermi surfaces as shown by the shaded areas in Fig. 4C, because all the Weyl nodes are type II. It is known that, at the energy of a type II Weyl node, the bulk Fermi surface is not an isolated point but a touching point between an electron and a hole pocket (*39*). The Fermi surface does not respect mirror symmetry along the $\bar{\Gamma}$-$\bar{X}$ or $\bar{\Gamma}$-$\bar{Y}$ axis. As shown in Fig. 4A, $\bar{\Gamma}$-$\bar{Y}$ is the projection of the $k_x = 0$ plane, which is not a mirror plane. $\bar{\Gamma}$-$\bar{X}$ is the projection of the $k_y = 0$ plane, which is indeed a mirror plane. However, it corresponds to a glide mirror operation $\mathcal{G}_y$: $(x, y, z) \Rightarrow (x, -y, z + 0.5)$. Therefore, the $(\bar{2}02)$ surface breaks the glide mirror symmetry. To visualize the Fermi arc surface states, Fig. 4B shows the energy dispersion cut along *Cut*1 (denoted by the red dashed line in Fig. 4A). In both box 1 and box 2, we clearly see that a surface state is terminated directly onto a Weyl node, which is the touching point between the shaded areas. This calculation demonstrates the existence of the Fermi arc surface states. Specifically, we label the two surface states in box 1 (upper right panel in Fig. 4B) as β and α from left to right. We see that β is the Fermi arc. In Fig. 4D, we show the high-resolution Fermi surface zoomed in near the $\bar{X}$ point. The Weyl node that corresponds to box 1 is the black dot that is directly above the bottom-leftmost black dot in Fig. 4D. The two surface states, α and β, are identified and, indeed, the left surface state, β, is the Fermi arc terminating onto this Weyl node. Through similar analyses, we can determine that α is the Fermi arc corresponding to the bottom-leftmost Weyl node. On the basis of the above analyses, we show the determined Fermi arc connection in Fig. 4E. We also emphasize that

Downloaded from http://advances.sciencemag.org/ on September 26, 2017

the topological band theory of the Weyl semimetal phase only requires that the number of Fermi arcs that are terminated on a given projected Weyl node must be equal to the absolute value of its chiral charge. The detailed connectivity pattern can vary based on surface conditions, such as surface potential, surface relaxation, and surface density. Hence, the purpose of Fig. 4E is to show the existence of Fermi arcs, which are a key signature of the Weyl semimetal state in Ta_3S_2. The details of the surface electronic structure, including the connectivity pattern, will depend on the surface conditions, which have to be determined by experiments.

Now, we show the topological metal-to-insulator transition in Ta_3S_2 in Fig. 5. To best visualize the transition, we show the band dispersion along a cut that goes through an irreducible pair of Weyl nodes (as defined by the red dashed line in Fig. 6D). As shown in Fig. 5A, we show this cut as a function of different values of the lattice constant b. At the original lattice constant $b' = b$, we indeed see a pair of type II Weyl nodes, as expected. As we increase the lattice constant by 3.0% ($b' = 1.030b$), we see that Weyl nodes approach each other and their separation decreases by half. As we further increase the lattice constant to $b' = 1.040b$, the two Weyl nodes annihilate each other and the band structure becomes fully gapped. By a careful calculation, we determined that the lattice constant corresponding to the critical point is $b' = 1.037b$. The resulting fully gapped state for $b' > 1.037b$ has two possible fates, that is, either a trivial

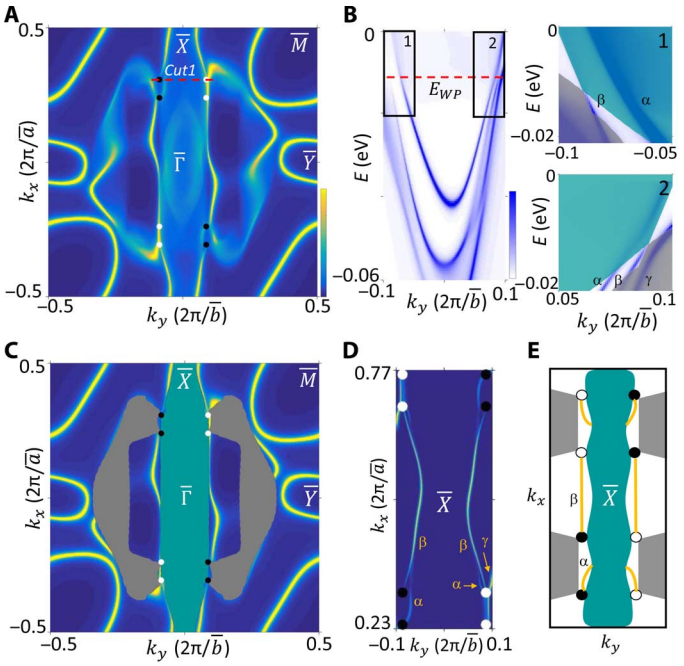

Fig. 4. Fermi arcs in Ta_3S_2. (**A**) Surface state spectrum for the ($\bar{2}02$) surface of Ta_3S_2 at constant energy. The surface states are shown in yellow. A finite amount of projected bulk Fermi surfaces is observed because of the type II character of the Weyl nodes. The projected Weyl nodes are denoted by black and white circles. (**B**) Energy dispersion cut along *Cut*1 (red dashed line) for a pair of projected Weyl nodes around $\bar{X}$ in (A). As a guide, the red dashed line represents the energy level of the Weyl node ($E_{W1} \approx -10$ meV). The left panel shows two surface states (blue curves) emerging from box 1 and three entering box 2. The top-rightmost panel is zoomed into box 1 and shows a touching point, which defines the Weyl node as type II and two Fermi arc surface states that are labeled α and β. The β Fermi arc surface state terminates onto the Weyl node. The bottom-rightmost panel is similar to the top-rightmost panel. Here, we observe three Fermi arc surface states, α, β, and γ. Again, the β Fermi arc surface state is observed to terminate onto the Weyl node. (**C**) Same as (A) but with the projected bulk bands represented by shaded areas. The Fermi arc surface states connecting pairs of projected Weyl nodes are distinguishable from the remaining trivial surface states. (**D**) Zoom-in of the surface states around the projected Weyl nodes near $\bar{X}$. Shown, among other things, are eight projected Weyl nodes. Single Fermi arc surface states, β, are shown to connect two individual pairs of Weyl nodes, which is consistent with the predicted ± 1 chiral charge for each Weyl node. The α and γ Fermi arc surface states described in (B) are also labeled. (**E**) Cartoon illustration of (D) showing a possible Fermi arc linking scheme. The exact connectivity pattern of Fermi arcs with Weyl nodes depends on the surface conditions.

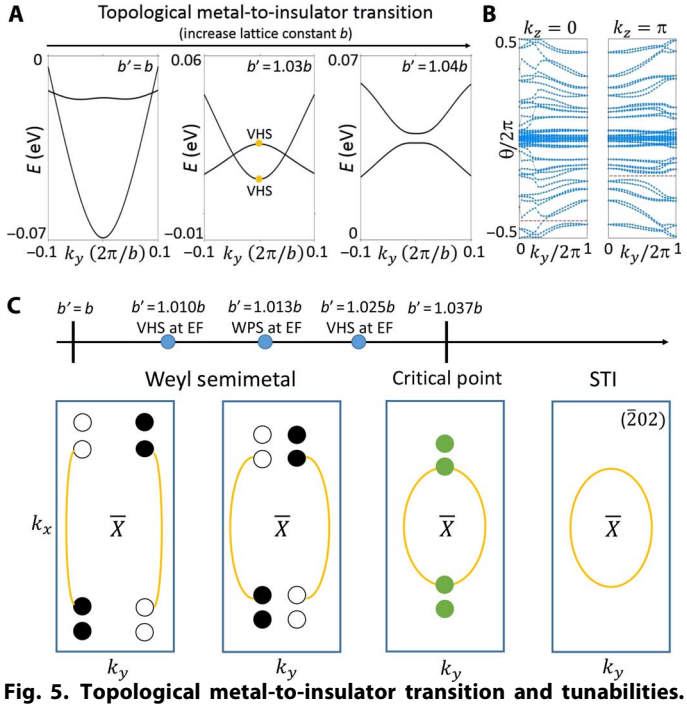

Fig. 5. Topological metal-to-insulator transition and tunabilities. (**A**) Energy dispersion cut along k_y for an irreducible pair of Weyl nodes as the b lattice constant is tuned to various values. At $b' = b$ (left panel), we observe a pair of type II Weyl nodes. At $b' = 1.03b$ (middle panel), the two Weyl nodes approach each other and their separation decreases by about half. Another important feature shown is the VHSs, which are labeled with yellow circles. At $b' \geq 1.04b$ (right panel), the two Weyl nodes annihilate each other and the band structure becomes fully gapped. (**B**) Calculation of the Wilson loop of the Wannier function centered in the $k_z = 0$ plane and in the $k_z = \pi$ plane is performed to confirm the strong topological insulator (STI) state. Red dashed lines are arbitrary reference positions. The left panel shows one band crossing the red dashed line, which corresponds to Z_2 invariant of 1 for the $k_z = 0$ plane. The right panel shows no band crossing the red dashed line, which corresponds to Z_2 invariant of 0 for the $k_z = \pi$ plane. $Z_2 = 1$ confirms the STI state in Ta_3S_2. (**C**) An illustration of the topological metal-to-insulator transition for the Weyl nodes around the $\bar{X}$ pocket on the ($\bar{2}02$) surface. Fermi arc surface states are shown in yellow. Because b' is tuned, the Weyl nodes reach the critical point at $b' = 1.037$ and the system becomes fully gapped for $b' > 1.037$ with a single topological surface state with the Fermi surface enclosing the Kramers' point $\bar{X}$, resulting in a topological insulator state. Furthermore, because b' is tuned from its original value, the VHSs arising from the Weyl cone reach the Fermi level when $b' = 1.01b$ and $b' = 1.025b$. The Weyl nodes reach the Fermi level when $b' = 1.013b$.

Downloaded from http://advances.sciencemag.org/ on September 26, 2017

insulator or a topological insulator. We have calculated the Wilson loop of the Wannier function centered on the $k_z = 0$ plane and on the $k_z = \pi$ plane (Fig. 5B), from which we determined that the gapped state for $b' > 1.037b$ is a topological insulator and its $\mathcal{Z}_2$ indices are (1; 000). Therefore, by increasing the lattice constant b, one can realize a topological phase transition from a Weyl semimetal state to a topological insulator state in Ta_3S_2. The corresponding evolution of the surface electronic structure is shown in Fig. 5C for the case of the $(\bar{2}02)$ surface. The projected Weyl nodes of opposite chirality, which are connected by the Fermi arcs, approach each other and eventually meet on the $\bar{X}$-$\bar{\Gamma}$ axis where they annihilate. The resulting surface has a single surface state whose Fermi surface encloses the Kramers point $\bar{X}$, which also demonstrates the topological insulator state.

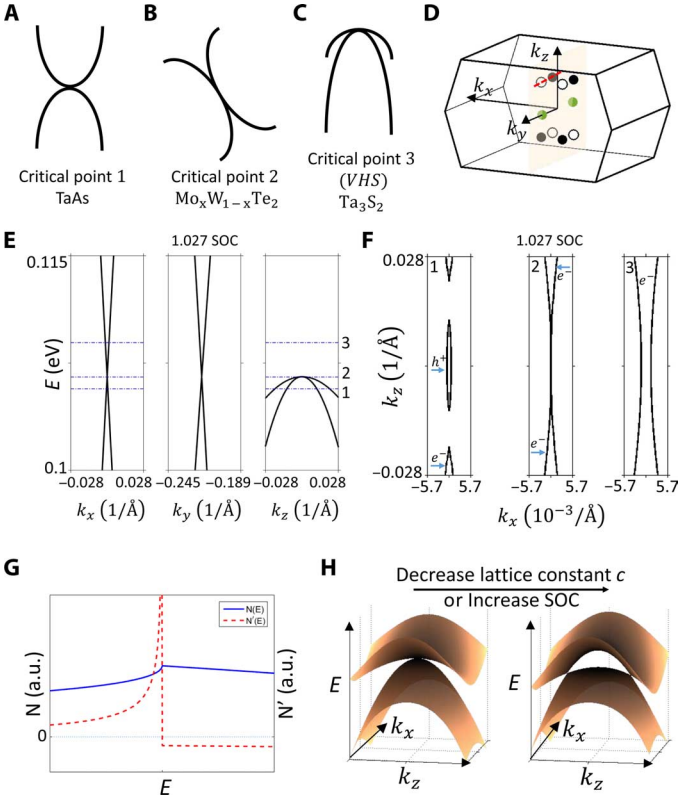

Fig. 6. New type of critical point. (**A**) Illustration of the critical point for TaAs as two opposite-facing parabolas are driven into each other. (**B**) Similar to (A) but for $Mo_xW_{1-x}Te_2$, which shows two opposite-facing parabolas that are tilted away from being vertical. (**C**) Ta_3S_2 shows two parabolas that face the same direction. This new type of critical point leads to a saddle point in the band structure and gives rise to a VHS. (**D**) The momentum space locations of the newly emerged band touchings resulting from driving the system's conduction and valence bands toward each other by changing SOC λ into the critical point $\lambda_{critical} = 1.027\ \lambda$, which are represented by the green dots. (**E**) The saddle point behavior is clearly demonstrated from the band dispersions for $\lambda_{critical} = 1.027\ \lambda$ by noting that the touching point for the conduction band along the k_x and k_y directions is at the energy minimum, whereas the touching point along the k_z direction is at the energy maximum. (**F**) The Fermi surfaces corresponding to energy levels 1, 2, and 3 along the k_x direction in the far-left panel in (E). (**G**) The saddle point band structure brings about the VHS, which generates a maxima in the DOS (N, blue solid line) and a divergence in the first derivative of the DOS (N', red dashed line) at the energy of the VHS. a.u., arbitrary units. (**H**) Illustrations of the conduction and valence bands along the k_z direction as the system is driven into its critical points by either decreasing the c to $c_{critical}$ lattice constant or increasing the SOC strength λ to $\lambda_{critical}$.

Besides the topological phase transition, we found that the system exhibits other important tunabilities. Specifically, it can be seen that although the Weyl nodes at the original lattice constant are type II, they become type I at $b' = 1.030b$, because the Weyl node is now formed by two bands with the opposite sign of velocity (Fig. 5A). Therefore, there is a transition from type II Weyl fermions to type I Weyl femions as one increases the lattice constant b. Moreover, we note that the energy of the bands in Fig. 5A shifts across the chemical potential as one increases b. Therefore, specific values of the lattice constant b also exist, at which important features will be moved exactly onto the chemical potential. We focus on two important features, that is, the Weyl nodes and the Van Hove singularities (VHSs) that arise from the Weyl cones (see the middle panel of Fig. 5A). Placing the Weyl nodes at the Fermi level is very meaningful because they are monopoles of Berry curvature. Thus, any novel phenomenon that arises from the chirality of the Weyl fermions, such as the chiral anomaly, will become most significant when the Weyl nodes are at the Fermi level. Putting the VHS at the Fermi level can also be interesting because the VHS is due to a saddle point in the band structure, which means that the DOS will show a maxima at the energy of the VHS. An enhanced DOS is favorable for inducing correlated physics, such as superconductivity or magnetism. A detailed phase diagram is shown in Fig. 5C.

We show that the band structure of Ta_3S_2 exhibits a new type of critical point as one decreases the lattice constant c or increases the SOC λ. As discussed above, under ambient conditions, the conduction and valence bands only touch each other at eight discrete points in the BZ, which are the eight Weyl nodes. Here, we show that decreasing the lattice constant c or increasing the SOC λ leads to the generation of new Weyl nodes. Representing the critical point for this process is the critical value for the lattice constant c or SOC λ corresponding to the point where the conduction and valence bands just touch, $c_{critical} = 0.98c$ or $\lambda_{critical} = 1.027\ \lambda$. Taking the critical point of $\lambda_{critical} = 1.027\ \lambda$ as the example, we show the k-space locations of these newly emerged band touchings by the green dots in Fig. 6D. We find that the critical point band structure is novel. Specifically, the dispersion along k_z near the band touching behaves like two downward-facing parabolas. These two parabolas touch at their vertex, which forms the band touching point. This is distinct from the critical points associated with any previously known Weyl semimetal candidates. For example, the critical point band structure of TaAs can be thought of as two parabolas of opposite directions, one facing up and the other facing down (Fig. 6A). Then, entering the Weyl phase from the critical point essentially means "pushing" the two parabolas "into" each other so that they cross to form the two Weyl nodes. The situation in the $Mo_xW_{1-x}Te_2$ system is very similar, the only difference being that the direction of the parabolas is titled away from being vertical (Fig. 6B). By contrast, in Ta_3S_2, we have two parabolas that face the same direction (Fig. 6C). A distinct and unique property of the new critical point is that it leads to a saddle point in the band structure, giving rise to a VHS. The saddle point behavior can be seen from the band dispersions shown in Fig. 6E. If one focuses on the conduction band in Fig. 6E, then the touching point is the energy minima for the dispersions along the k_x, k_y directions, but it is the energy maxima along the k_z direction. The saddle point band structure brings about a VHS, which generates a maxima in the DOS and a divergence

Downloaded from http://advances.sciencemag.org/ on September 26, 2017

in the first derivative of the DOS at the energy of the VHS, as shown in Fig. 6G.

DISCUSSION

We elaborate the meaning of the robust and ideal Weyl semimetal candidate as emphasized in our paper. First, we mean that the realization of the candidate is likely to be experimentally feasible. This involves the following critical conditions: (i) the prediction is based on the realistic crystal structure, which means that the compound does crystallize in the proposed crystal structure under ambient conditions; (ii) the prediction does not require fine-tuning of the chemical composition or the magnetic domains; and (iii) the Weyl nodes are not located at energies far above the chemical potential such that they can be observed by photoemission. This was the case for our prediction of TaAs (*17*), which has now been realized (*19*). This is also the case here for Ta_3S_2, which demonstrates the experimental feasibility of our proposal on Ta_3S_2. Second, and more importantly, the term "robust" also refers to a large separation of the Weyl nodes in momentum space because, as discussed above, the separation of the Weyl nodes provides a measure of a Weyl semimetal's topological strength. We again highlight that Ta_3S_2 has the largest k-space separation between Weyl nodes among known Weyl semimetal candidates, which is about twice larger than that of TaAs. This will greatly help resolve the Weyl nodes in various spectroscopic measurements, such as photoemission and scanning tunneling spectroscopy. This will also make it easier to probe the chiral anomaly and other Berry curvature monopole physics in electrical and optical transport experiments.

Finally, we compare the topological metal-to-insulator transition in Ta_3S_2 with transitions predicted in other Weyl candidates (*44*, *45*). Theoretical work by Nozaki *et al.* (*43*) predicted the topological phase transitions from a trivial band insulator to a Weyl semimetal and then to a topological insulator by varying the chemical composition x in $LaBi_{1-x}Sb_xTe_3$ or applying external pressure to BiTeI. However, the composition or pressure range that corresponds to the Weyl semimetal phase is predicted to be extremely narrow (*43*). Hence, it requires ultra–fine-tuning, which is very difficult in experiments. Also, $LaBi_{1-x}Sb_xTe_3$ has never been grown in the crystal structure required by the proposal of Nozaki *et al.* (*43*) at least in the single-crystal form. The work by Liu *et al.* (*45*) proposed similar transitions in the β-Bi_4Br_4 under external pressure. To induce a Weyl semimetal phase in the β-Bi_4Br_4 crystal structure that has inversion symmetry, a hypothetical inversion-breaking term was assumed in the calculation. By contrast, Ta_3S_2 is an inversion-breaking, single-crystalline compound. Single-crystalline Ta_3S_2 samples have been grown (*42*, *43*). The Weyl semimetal state is stable and does not require fine-tuning. We propose the following three methods for increasing the b lattice constant: (i) It can be achieved by applying external force. The method has been demonstrated by Zheng *et al.* (*46*). As an order-of-magnitude estimate, we calculated the required force by first-principles calculations and obtained an approximately 6-GPa force for an approximately 4% increase in the b lattice constant. Force in this range is experimentally feasible and the change of the lattice constant can be monitored by transmission electron microscopy (*46*). (ii) It may also be achieved by growing a Ta_3S_2 film onto a substrate with lattice mismatch. (iii) It may be achieved by growing samples with isoelectronic chemical substitution, such as $Ta_3(S_{1-x}Se_x)_2$. These facts highlight that Ta_3S_2 is, to date, the most ideal platform not only for advancing our understanding of Weyl semimetals and Weyl physics but also for facilitating the exploitation of the exotic and novel properties in future device applications.

MATERIALS AND METHODS

First-principles calculations of Ta_3S_2 were performed using the OpenMX code based on norm-conserving pseudopotentials generated with multireference energies and optimized pseudoatomic basis functions (*47*, *48*). The SOC was incorporated through j-dependent pseudopotentials, and the generalized gradient approximation was adopted for the exchange-correlation energy functional (*49*, *50*). For each Ta atom, three, two, two, and one optimized radial function were allocated for the s, p, d, and f orbitals ($s3p2d2f1$), respectively. For each S atom, $s3p2d2f1$ was adopted. The cutoff radius for both Ta and S basis functions was 7 bohr, and the cutoff energy was 1000 rydberg. A k-point mesh of $13 \times 11 \times 11$ for the primitive unit cell and the experimental lattice parameters were adopted in the calculations. We used the Ta d and S p orbitals to construct the Wannier functions. We calculated the surface spectral weight of a semi-infinite $(\bar{2}02)$ slab using the iterative Green's function method from the Wannier function–based tight-binding model. We did not choose the (001) and the (010) surfaces because pairs of Weyl nodes of opposite chirality are projected onto each other on these two surfaces (Fig. 3B). Hence, the (001) and the (010) surfaces do not carry net-projected chiral charge and are not expected to show Fermi arcs. Because the purpose of the surface calculations (Fig. 4) was to demonstrate the existence of Fermi arcs, the usage of the $(\bar{2}02)$ surface is proper and sufficient.

SUPPLEMENTARY MATERIALS

Supplementary material for this article is available at http://advances.sciencemag.org/cgi/content/full/2/6/e1600295/DC1

Supplementary Text

fig. S1. Fermi arc surface states and Weyl nodes on the $(\bar{2}02)$ surface without SOC.

fig. S2. Distribution of Weyl nodes in Ta_3S_2.

REFERENCES AND NOTES

1. F. Wilczek, Why are there analogies between condensed matter and particle theory? *Phys. Today* **51**, 11–13 (1998).
2. A. K. Geim, K. S. Novoselov, The rise of graphene. *Nat. Mater.* **6**, 183–191 (2007).
3. M. Z. Hasan, C. L. Kane, Colloquium: Topological insulators. *Rev. Mod. Phys.* **82**, 3045–3067 (2010).
4. X.-L. Qi, S.-C. Zhang, Topological insulators and superconductors. *Rev. Mod. Phys.* **83**, 1057–1110 (2011).
5. M. Z. Hasan, J. E. Moore, Three-dimensional topological insulators. *Annu. Rev. Condens. Matter Phys.* **2**, 55–78 (2011).
6. H. Weyl, Elektron und gravitation. I. *Z. Phys.* **56**, 330–352 (1929).
7. C. Herring, Accidental degeneracy in the energy bands of crystals. *Phys. Rev.* **52**, 365–373 (1937).
8. A. A. Abrikosov, S. D. Beneslavskii, Some properties of gapless semiconductors of the second kind. *J. Low Temp. Phys.* **5**, 141–154 (1971).
9. H. B. Nielsen, M. Ninomiya, The Adler-Bell-Jackiw anomaly and Weyl fermions in a crystal. *Phys. Lett. B* **130**, 389–396 (1983).
10. G. E. Volovik, *The Universe in a Helium Droplet* (Oxford Univ. Press, 2003).
11. S. Murakami, Phase transition between the quantum spin Hall and insulator phases in 3D: Emergence of a topological gapless phase. *New J. Phys.* **9**, 356 (2007).
12. X. Wan, A. M. Turner, A. Vishwanath, S. Y. Savrasov, Topological semimetal and Fermi-arc surface states in the electronic structure of pyrochlore iridates. *Phys. Rev. B* **83**, 205101 (2011).
13. K.-Y. Yang, Y.-M. Lu, Y. Ran, Quantum Hall effects in a Weyl semimetal: Possible application in pyrochlore iridates. *Phys. Rev. B* **84**, 075129 (2011).
14. L. Balents, Viewpoint: Weyl electrons kiss. *Phys. Chem* **4**, 36 (2011).

Downloaded from http://advances.sciencemag.org/ on September 26, 2017

15. A. A. Burkov, L. Balents, Weyl semimetal in a topological insulator multilayer. *Phys. Rev. Lett.* **107**, 127205 (2011).
16. S.-Y. Xu, C. Liu, S. K. Kushwaha, R. Sankar, J. W. Krizan, I. Belopolski, M. Neupane, G. Bian, N. Alidoust, T.-R. Chang, H.-T. Jeng, C.-Y. Huang, W.-F. Tsai, H. Lin, P. P. Shibayev, F.-C. Chou, R. J. Cava, M. Z. Hasan, Observation of Fermi arc surface states in a topological metal. *Science* **347**, 294–298 (2015).
17. S.-M. Huang, S.-Y. Xu, I. Belopolski, C.-C. Lee, G. Chang, B. Wang, N. Alidoust, G. Bian, M. Neupane, C. Zhang, S. Jia, A. Bansil, H. Lin, M. Z. Hasan, A Weyl fermion semimetal with surface Fermi arcs in the transition metal monopnictide TaAs class. *Nat. Commun.* **6**, 7373 (2015).
18. H. Weng, C. Fang, Z. Fang, B. A. Bernevig, X. Dai, Weyl semimetal phase in noncentrosymmetric transition-metal monophosphides. *Phys. Rev. X* **5**, 011029 (2015).
19. S.-Y. Xu, I. Belopolski, N. Alidoust, M. Neupane, G. Bian, C. Zhang, R. Sankar, G. Chang, Z. Yuan, C.-C. Lee, S.-M. Huang, H. Zheng,J. Ma, D. S. Sanchez, B. Wang, A. Bansil, F. Chou, P. P. Shibayev, H. Lin, S. Jia, M. Z. Hasan, Discovery of a Weyl fermion semimetal and topological Fermi arcs. *Science* **349**, 613–617 (2015).
20. L. Lu, Z. Wang, D. Ye, L. Ran, L. Fu, J. D. Joannopoulos, M. Soljačić, Experimental observation of Weyl points. *Science* **349**, 622–624 (2015).
21. B. Q. Lv, H. M. Weng, B. B. Fu, X. P. Wang, H. Miao, J. Ma, P. Richard, X. C. Huang, L. X. Zhao, G. F. Chen, Z. Fang, X. Dai, T. Qian, H. Ding, Experimental discovery of Weyl semimetal TaAs. *Phys. Rev. X* **5**, 031013 (2015).
22. X. Huang, L. Zhao, Y. Long, P. Wang, D. Chen, Z. Yang, H. Liang, M. Xue, H. Weng, Z. Fang, X. Dai, G. Chen, Observation of the chiral anomaly induced negative magneto-resistance in 3D Weyl semi-metal TaAs. *Phys. Rev. X* **5**, 031023 (2015).
23. C. Zhang, S.-Y. Xu, I. Belopolski, Z. Yuan, Z. Lin, B. Tong, N. Alidoust, C.-C. Lee, S.-M. Huang, H. Lin, M. Neupane, D. S. Sanchez, H. Zheng, G. Bian, J. Wang, C. Zhang, T. Neupert, M. Z. Hasan, S. Jia, Observation of the Adler-Bell-Jackiw chiral anomaly in a Weyl semimetal. arXiv:1503.02630 (2015).
24. C. Zhang, Z. Yuan, S. Xu, Z. Lin, B. Tong, M. Zahid Hasan, J. Wang, C. Zhang, S. Jia, Tantalum monoarsenide: An exotic compensated semimetal. arXiv:1502.00251 (2015).
25. P. Hosur, X. Qi, Z. Fang, X.-L. Qi, Time-reversal invariant topological superconductivity in doped Weyl semimetals. *Phys. Rev. B* **90**, 045130 (2014).
26. G. Bednik, A. A. Zyuzin, A. A. Burkov, Superconductivity in Weyl semimetals. *Phys. Rev. B* **92**, 035153 (2015).
27. Y. Li, F. D. M. Haldane, Topological nodal Cooper pairing in doped Weyl metals. arXiv:1510.01730 (2015).
28. B. Q. Lv, N. Xu, H. M. Weng, J. Z. Ma, P. Richard, X. C. Huang, L. X. Zhao, G. F. Chen, C. E. Matt, F. Bisti, V. N. Strocov, J. Mesot, Z. Fang, X. Dai, T. Qian, M. Shi, H. Ding, Observation of Weyl nodes in TaAs. *Nat. Phys.* **11**, 724–727 (2015).
29. L. X. Yang, Z. K. Liu, Y. Sun, H. Peng, H. F. Yang, T. Zhang, B. Zhou, Y. Zhang, Y. F. Guo, M. Rahn, D. Prabhakaran, Z. Hussain, S.-K. Mo, C. Felser, B. Yan, Y. L. Chen, Erratum: Weyl semimetal phase in the non-centrosymmetric compound TaAs. *Nat. Phys.* **11**, 879 (2015).
30. S.-Y. Xu, N. Alidoust, I. Belopolski, Z. Yuan, G. Bian, T.-R. Chang, H. Zheng, V. N. Strocov, D. S. Sanchez, G. Chang, C. Zhang, D. Mou, Y. Wu, L. Huang, C.-C. Lee, S.-M. Huang, B. K. Wang, A. Bansil, H.-T. Jeng, T. Neupert, A. Kaminski, H. Lin, S. Jia, M. Z. Hasan, Discovery of a Weyl fermion state with Fermi arcs in niobium arsenide. *Nat. Phys.* **11**, 748–754 (2015).
31. S.-Y. Xu, I. Belopolski, D. S. Sanchez, C. Zhang, G. Chang, C. Guo, G. Bian, Z. Yuan, H. Lu, T.-R. Chang, P. P. Shibayev, M. L. Prokopovych, N. Alidoust, H. Zheng, C.-C. Lee, S.-M. Huang, R. Sankar, F. Chou, C.-H. Hsu, H.-T. Jeng, A. Bansil, T. Neupert, V. N. Strocov, H. Lin, S. Jia, M. Z. Hasan, Experimental discovery of a topological Weyl semimetal state in TaP. *Sci. Adv.* **1**, e1501092 (2015).
32. N. Xu, H. M. Weng, B. Q. Lv, C. E. Matt, J. Park, F. Bisti, V. N. Strocov, D. Gawryluk, E. Pomjakushina, K. Conder, N. C. Plumb, M. Radovic, G. Autès, O. V. Yazyev, Z. Fang, X. Dai, T. Qian, J. Mesot, H. Ding, M. Shi, Observation of Weyl nodes and Fermi arcs in tantalum phosphide. *Nat. Commun.* **7**, 11006 (2016).
33. D. F. Xu, Y. P. Du, Z. Wang, Y. P. Li, X. H. Niu, Q. Yao, P. Dudin, Z.-A. Xu, X. G. Wan, D. L. Feng, Observation of Fermi arcs in non-centrosymmetric Weyl semi-metal candidate NbP. *Chin. Phys. Lett.* **32**, 107101 (2015).
34. I. Belopolski, S.-Y. Xu, D. Sanchez, G. Chang, C. Guo, M. Neupane, H. Zheng, C.-C. Lee, S.-M. Huang, G. Bian, N. Alidoust, T.-R. Chang, B. Wang, X. Zhang, A. Bansil, H.-T. Jeng, H. Lin, S. Jia, M. Z. Hasan, Criteria for directly detecting topological Fermi arcs in Weyl semimetals. *Phys. Rev. Lett.* **116**, 066802 (2016).
35. S. Souma, Z. Wang, H. Kotaka, T. Sato, K. Nakayama, Y. Tanaka, H. Kimizuka, T. Takahashi, K. Yamauchi, T. Oguchi, K. Segawa, Y. Ando, Direct observation of nonequivalent Fermi-arc states of opposite surfaces in noncentrosymmetric Weyl Semimetal NbP. *Phys. Rev. B* **93**, 161112 (2015).
36. Z. K. Liu, L. X. Yang, Y. Sun, T. Zhang, H. Peng, H. F. Yang, C. Chen, Y. Zhang, Y. F. Guo, D. Prabhakaran, M. Schmidt, Z. Hussain, S.-K. Mo, C. Felser, B. Yan, Y. L. Chen, Evolution of the Fermi surface of Weyl semimetals in the transition metal pnictide family. *Nat. Mater.* **15**, 27–31 (2016).
37. H. Zheng, S.-Y. Xu, G. Bian, C. Guo, G. Chang, D. S. Sanchez, I. Belopolski, C.-C. Lee, S.-M. Huang, X. Zhang, R. Sankar, N. Alidoust, T.-R. Chang, F. Wu, T. Neupert, F. Chou, H.-T. Jeng, N. Yao, A. Bansil, S. Jia, H. Lin, M. Z. Hasan, Atomic-scale visualization of quantum interference on a Weyl semimetal surface by scanning tunneling microscopy. *ACS Nano* **10**, 1378–1385 (2016).
38. T.-R. Chang, S.-Y. Xu, G. Chang, C.-C. Lee, S.-M. Huang, B. Wang, G. Bian, H. Zheng, D. S. Sanchez, I. Belopolski, N. Alidoust, M. Neupane, A. Bansil, H.-T. Jeng, H. Lin, M. Zahid Hasan, Arc-tunable Weyl fermion metallic state in $Mo_xW_{1-x}Te_2$. *Nat. Commun.* **7**, 10639 (2016).
39. A. A. Soluyanov, D. Gresch, Z. Wang, Q. Wu, M. Troyer, X. Dai, B. A. Bernevig, Type-II Weyl semimetals. *Nature* **527**, 495–498 (2015).
40. S.-Y. Xu, N. Alidoust, G. Chang, H. Lu, B. Singh, I. Belopolski, D. Sanchez, X. Zhang, G. Bian, H. Zheng, M.-A. Husanu, Y. Bian, S.-M. Huang, C.-H. Hsu, T.-R. Chang, H.-T. Jeng, A. Bansil, V. N. Strocov, H. Lin, S. Jia, M. Zahid Hasan, Discovery of Lorentz-violating Weyl fermion semimetal state in LaAlGe materials. arXiv:1603.07318 (2016).
41. H. Isobe, N. Nagaosa, Coulomb interaction effect in Weyl fermions with tilted energy dispersion in two dimensions. *Phys. Rev. Lett.* **116**, 116803 (2016).
42. S. J. Kim, K. S. Nanjundaswamy, T. Hughbanks, Single-crystal structure of tantalum sulfide (Ta_3S_2). Structure and bonding in the Ta_6Sn (n = 1, 3, 4, 5?) pentagonal-antiprismatic chain compounds. *Inorg. Chem.* **30**, 159–164 (1991).
43. H. Nozaki, H. Wada, S. Takekawa, Galvanomagnetic properties of Ta_3S_2, Ta_2S and Ta_6S. *J. Phys. Soc. Jpn.* **60**, 3510–3515 (1991).
44. J. Liu, D. Vanderbilt, Weyl semimetals from noncentrosymmetric topological insulators. *Phys. Rev. B* **90**, 155316 (2014).
45. C.-C. Liu, J.-J. Zhou, Y. Yao, F. Zhang, Weak topological insulators and composite Weyl semimetals: β–Bi_4 X_4(X=Br, I. *Phys. Rev. Lett.* **116**, 066801 (2016).
46. H. Zheng, A. Cao, C. R. Weinberger, J. Y. Huang, K. Du, J. Wang, Y. Ma, Y. Xia, S. X. Mao, Discrete plasticity in sub-10-nm-sized gold crystals. *Nat. Commun.* **1**, 144 (2010).
47. T. Ozaki, Variationally optimized atomic orbitals for large-scale electronic structures. *Phys. Rev. B* **67**, 155108 (2003).
48. T. Ozaki, H. Kino, J. Yu, M. J. Han, M. Ohfuchi, F. Ishii, K. Sawada, Y. Kubota, T. Ohwaki, H. Weng, M. Toyoda, Y. Okuno, R. Perez, P. P. Bell, T. V. T. Duy, Y. Xiao, A. M. Ito, K. Terakura, OpenMX V.3.7. (2013).
49. G. Theurich, N. A. Hill, Self-consistent treatment of spin-orbit coupling in solids using relativistic fully separable ab initio pseudopotentials. *Phys. Rev. B* **64**, 073106 (2001).
50. J. P. Perdew, K. Burke, M. Ernzerhof, Generalized gradient approximation made simple. *Phys. Rev. Lett.* **77**, 3865–3868 (1996).

Acknowledgments

Funding: Work at Princeton University was supported by the U.S. Department of Energy (DOE), Office of Science, Basic Energy Sciences (BES), under DE-FG-02-05ER46200. Work at the National University of Singapore was supported by the National Research Foundation (NRF), Prime Minister's Office, Singapore, under its NRF fellowship (NRF award no. NRF-NRFF2013-03). T.-R.C. and H.-T.J. were supported by the National Science Council, Taiwan. H.-T.J. also thanks the National Center for High-Performance Computing, Computer and Information Network Center, National Taiwan University, and the National Center for Theoretical Sciences, Taiwan, for technical support. Work at Northeastern University was supported by U.S. DOE/BES grant no. DE-FG02-07ER46352 and benefited from Northeastern University's Advanced Scientific Computation Center and the National Energy Research Scientific Computing Center supercomputing center through DOE grant no. DE-AC02-05CH11231. S.M.H., G.C., and T.R.C. acknowledge their visiting scholar positions at Princeton University, which were funded by the Gordon and Betty Moore Foundation EPiQS Initiative through grant GBMF4547 (Hasan). **Author contributions:** Preliminary material search and analysis were performed by S.-Y.X. Theoretical analysis and computations were performed by G.C., S.-M.H., C.-C.L., T.-R.C., H.-T.J., A.B., and H.L. G.C. made the figures with help from S.-Y. X. S.-Y.X. wrote the article with major help from G.C., D.S.S., and H.L. G.B., H.Z., I.B., and N.A. helped in general with the theoretical analysis and the proof checking of the article. H.L. supervised the theoretical part of the work. M.Z.H. was responsible for the overall direction, planning, and integration among different research units. **Competing interests:** The authors declare that they have no competing interests. **Data and materials availability:** All data needed to evaluate the conclusions in the paper are present in the paper and/or the Supplementary Materials. Additional data related to this paper may be requested from the authors.

Submitted 11 February 2016
Accepted 23 May 2016
Published 24 June 2016
10.1126/sciadv.1600295

Citation: G. Chang, S.-Y. Xu, D. S. Sanchez, S.-M. Huang, C.-C. Lee, T.-R. Chang, G. Bian, H. Zheng, I. Belopolski, N. Alidoust, H.-T. Jeng, A. Bansil, H. Lin, M. Z. Hasan, A strongly robust type II Weyl fermion semimetal state in Ta_3S_2. *Sci. Adv.* **2**, e1600295 (2016).

Downloaded from http://advances.sciencemag.org/ on September 26, 2017

Science Advances

A strongly robust type II Weyl fermion semimetal state in Ta_3S_2

Guoqing Chang, Su-Yang Xu, Daniel S. Sanchez, Shin-Ming Huang, Chi-Cheng Lee, Tay-Rong Chang, Guang Bian, Hao Zheng, Ilya Belopolski, Nasser Alidoust, Horng-Tay Jeng, Arun Bansil, Hsin Lin and M. Zahid Hasan

Sci Adv **2** (6), e1600295.
DOI: 10.1126/sciadv.1600295

ARTICLE TOOLS http://advances.sciencemag.org/content/2/6/e1600295

SUPPLEMENTARY MATERIALS http://advances.sciencemag.org/content/suppl/2016/06/21/2.6.e1600295.DC1

REFERENCES This article cites 44 articles, 4 of which you can access for free
http://advances.sciencemag.org/content/2/6/e1600295#BIBL

PERMISSIONS http://www.sciencemag.org/help/reprints-and-permissions

Use of this article is subject to the Terms of Service

Science Advances (ISSN 2375-2548) is published by the American Association for the Advancement of Science, 1200 New York Avenue NW, Washington, DC 20005. 2017 © The Authors, some rights reserved; exclusive licensee American Association for the Advancement of Science. No claim to original U.S. Government Works. The title *Science Advances* is a registered trademark of AAAS.

Downloaded from http://advances.sciencemag.org/ on September 26, 2017